AIAA JOURNAL
Vol. 58, No. 5, May 2020

Quad-Rotor Flight Simulation in Realistic Atmospheric Conditions

Behdad Davoudi,* Ehsan Taheri,† Karthik Duraisamy,‡ Balaji Jayaraman,§ and Ilya Kolmanovsky¶
University of Michigan, Ann Arbor, Michigan 48109

https://doi.org/10.2514/1.J058327

In trajectory planning and control design for unmanned air vehicles, highly simplified models are typically used to represent the vehicle dynamics and the operating environment. The goal of this work is to perform real-time, but realistic, flight simulations and trajectory planning for quad-copters in low-altitude (<500 m) atmospheric conditions. The aerodynamic model for rotor performance is adapted from blade element momentum theory and validated against experimental data. Large-eddy simulations of the atmospheric boundary layer are used to accurately represent the operating environment of unmanned air vehicles. A reduced-order version of the atmospheric boundary-layer data as well as the popular Dryden model are used to assess the impact of accuracy of the wind-field model on the predicted vehicle performance and trajectory. The wind model, aerodynamics, and control modules are integrated into a six-degree-of-freedom flight simulation environment with a fully nonlinear flight controller. Simulations are performed for two representative flight paths, namely, straight and circular paths. Results for different wind models are compared and the impact of simplifying assumptions in representing rotor aerodynamics is discussed. The simulation framework and codes are open sourced for use by the community.

Nomenclature

C_{d_0}	=	profile drag coefficient
C_l	=	two-dimensional lift coefficient
C_{l_α}	=	two-dimensional lift curve slope
C_P	=	power coefficient, $P/(\rho\pi R^5\omega^3)$
C_Q	=	torque coefficient, $Q/(\rho\pi R^5\omega^2)$
C_T	=	thrust coefficient, $T/(\rho\pi R^4\omega^2)$
C_W	=	weight coefficient, $W/(\rho\pi R^4\omega^2)$
c	=	rotor chord, m
$\bar{c}_d$	=	lumped drag coefficient
$\boldsymbol{D}$	=	drag, N
N_b	=	number of blades
p, q, r	=	body angular rates, rad $\cdot$ s^{-1}
R	=	rotor radius, m
Re	=	Reynolds number, Vc/ν
r	=	radial distance of a rotor spanwise station, m
$\boldsymbol{r}$	=	$[x, y, z]^T$ inertial position vector, m
T	=	total thrust, N
T_i	=	thrust of rotor i, N
$\boldsymbol{V}$	=	velocity in inertial frame, m $\cdot$ s^{-1}
$\boldsymbol{V}_{\text{rel}_B}$	=	velocity of the quad-copter with respect to wind represented in body frame, $\boldsymbol{V} - \boldsymbol{V}_W$, m $\cdot$ s^{-1}
V_{tip}	=	rotor tip velocity, m $\cdot$ s^{-1}
$\boldsymbol{V}_W$	=	wind velocity in inertial frame, m $\cdot$ s^{-1}
W	=	weight of the quad-copter, kg
α	=	sectional angle of attack, rad
Θ	=	blade pitch, rad
λ	=	rotor inflow ratio
λ_c	=	climb ratio
μ	=	advance ratio, $\sqrt{V_{\text{rel}_{B_x}}^2 + V_{\text{rel}_{B_y}}^2}/V_{\text{tip}}$
ν	=	kinematic viscosity, m^2 $\cdot$ s^{-1}
ρ	=	air density, kg $\cdot$ m^{-3}
σ	=	blade solidity, (blade area)/(rotor area)
τ_x, τ_y, τ_z	=	torque components in body frame (roll, pitch, and yaw torques, respectively), N $\cdot$ m
Φ	=	inflow angle, rad
Ψ	=	azimuth angle, rad
ψ, θ, ϕ	=	yaw, pitch, and roll, Euler angles, rad
ω	=	rotor angular velocity, rad $\cdot$ s^{-1}

Received 2 March 2019; revision received 7 December 2019; accepted for publication 19 February 2020; published online 31 March 2020.

*Ph.D. Candidate, Department of Aerospace Engineering.
†Postdoctoral Fellow, Department of Aerospace Engineering; currently Assistant Professor of Aerospace Engineering, Auburn University.
‡Associate Professor, Department of Aerospace Engineering.
§Visiting Researcher, Department of Aerospace Engineering; currently Assistant Professor of Mechanical and Aerospace Engineering, Oklahoma State University.
¶Professor, Department of Aerospace Engineering.

I. Introduction

OVER the past decade, small unmanned aerial systems (SUASs) (or drones) [1] have been increasingly used in a variety of tasks, including border patrolling [2], damage inspection [3], mapping [4], and precision agriculture [5]. With newer designs and mission profiles, simulation tools are required for assessing vehicle performance improvement [6–8], implications of atmospheric winds [9,10], aerodynamic force modeling [11], rotor failure studies [12], real-time flight simulation [13], and trajectory prediction and validation, especially in the context of certification by analysis [14].

Depending on the stage and/or nature of the study, various simplifications are invoked to facilitate the task of trajectory prediction and performance analysis [15–17]. Simplified atmospheric models are typically used for mission planning and certification of unmanned air vehicles (UAVs). In practice, the operating environment of UAVs flying at low altitudes (<500 m) is not only subject to strong mean velocity gradients (shear), but also involves intermittent unsteady wind gusts that contain a nontrivial fraction of energy compared with the mean flow. Further, the characteristic size of the turbulent eddies, even in a stable boundary layer, is on the order of a few meters [18], which is equivalent to the size of an SUAS. Accounting for such scales becomes critical to the vehicle aeromechanics, and thus to more accurate trajectory prediction and validation tasks.

A widely used tool for numerical weather prediction is the weather research and forecasting (WRF) model [19,20]. Weather research and forecasting is, however, a mesoscale model and is typically used over large spatial domains [$\mathcal{O}(1000)$ km] and with coarse resolutions [$\mathcal{O}(2)$ km]. Thus, WRF cannot be relied upon to represent all eddies and gusts of interest for SUAS trajectory prediction and validation purposes, and thus, a different higher-resolution approach is required.

It is a common practice to use idealized static models (i.e., simple algebraic models) to facilitate numerical analyses. However, these models do not capture the realistic performance of a propeller, which, in general, depends on the inflow velocity, and more accurate models are needed [21]. On the other hand, the use of higher-fidelity models, such as those based on computational fluid dynamics (CFD) [22–27], or even vortex-based methods [28,29] to predict the aeromechanics of flight vehicles is computationally demanding, and thus is not feasible

in trajectory optimization or trajectory prediction settings. As a consequence, an additional challenge is to establish a set of computationally efficient and effective models for the aeromechanics and flight dynamics of the SUAS vehicles.

The main contribution of this paper is to present efficient and accurate models of atmospheric conditions and vehicle aeromechanics, with the goal of using them in real-time trajectory planning, validation, and control. Specifically, the operating environment is characterized via atmospheric boundary-layer simulations. Aeromechanical models of appropriate fidelity are derived using momentum and blade element theories with an emphasis on low-altitude flight. These models are integrated within a numerical simulation environment that propagates a six-degree-of-freedom (DOF) model of a quad-copter along two representative nominal flight trajectory profiles: 1) an ascent–straight–descent profile and 2) a circular path. In addition, the trajectory of the quad-copter is controlled using a fully nonlinear backstepping control algorithm. Results from different wind models and propeller models are compared and discussed, highlighting the importance of modeling fidelity for realistic trajectory planning, validation, and control.

The remainder of the paper is organized as follows. Section II introduces the atmospheric boundary-layer model. Section III presents a review of the aerodynamic model. Section IV discusses the details of a fully nonlinear flight controller (namely, translational–rotational control algorithm). In Sec. V, the coupling between the aerodynamic models and control module is presented. Aerodynamic, dynamic, control, and wind models are integrated, and flight simulation results for a variety of problems are performed and presented in Sec. VI. Section VII provides a summary and conclusions.

II. Modeling Atmospheric Gust Effects

A. Atmospheric Boundary-Layer Simulation Using Large-Eddy Simulation

The popular approach to represent atmospheric gusts in aviation applications, such as trajectory estimation, relies on stochastic formulations [30,31] and its variants [32], all of which incorporate knowledge of the canonical spectral energy function [33]. Although computationally efficient, such methods have two major limitations: 1) use of parameterized equilibrium phenomenology that is often inaccurate, and 2) not explicitly accounting for the structure of the spectral energy tensor. In reality, the atmospheric boundary layer (ABL) turbulence is characterized by a strong and highly coherent eddying structure that contributes to the uncertainty associated with the predicted trajectory. Such limitations in wind forecasting for air traffic management are well known, as discussed in [34]. In a more recent study, Galway et al. [35] show that eddy-resolving CFD wind fields can cause significant trajectory effects to unmanned rotorcrafts. In this study, we build on this direction and adopt scientifically accurate, high-fidelity large-eddy simulations (LESs) of the ABL that capture energy-containing turbulence eddying structures at scales that are dynamically important for unmanned aerial flight.

The canonical ABL used to generate the wind-model data for this study is modeled as a rough flat wall boundary layer with surface heating from solar radiation, forced by a geostrophic wind in the horizontal plane, and solved in the rotational frame of reference fixed to Earth's surface. The lower troposphere sets the upper height limit for ABL, and is represented with a capping inversion and the mesoscale effects through a forcing geostrophic wind vector. The planetary boundary layer is different from engineering turbulent boundary layers in three major ways:

1) Coriolis effect: the rotation of Earth causes the surface to move relative to the fluid in the ABL that results in angular displacement of the mean wind vector that changes with height.

2) Buoyancy-driven turbulence: the diurnal heating of the surface generates buoyancy-driven temperature fluctuations that interact with the near-surface turbulent streaks to produce turbulent motions.

3) Capping inversion: a layer with strong thermal gradients that caps the microscale turbulence from interacting with the mesoscale weather eddies.

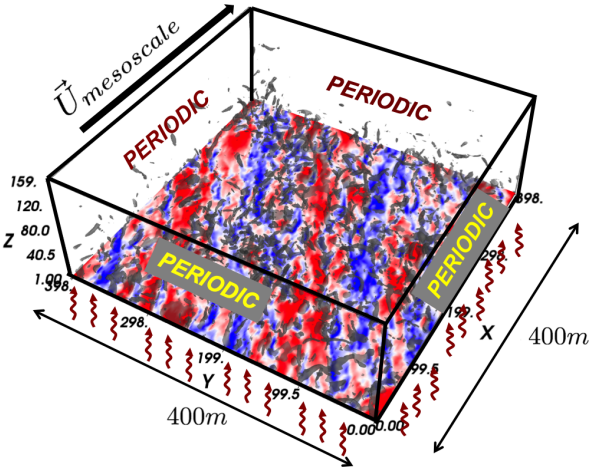

Fig. 1 Schematic showing the Coriolis effect in a three-dimensional visualization of ABL turbulence for a neutral ABL with $-z_i/L = 0$ using LES.

In Fig. 1, the mesoscale wind drives the ABL along the x direction while the rotation of Earth's surface orients the surface layer turbulence to nearly 30 deg relative to the imposed wind vector (along the streaks). The isosurfaces (gray) show vorticity magnitude at a value of 0.45 s^{-1}, and the isocontours show the horizontal fluctuating velocity. The blue regions denote low-speed streaks, whereas the red regions represent high-speed streaks.

1. *LES Methodology and Simulation Design*

The Reynolds number of the daytime ABL is extremely large. Hence, only the most energetic atmospheric turbulence motions are resolved. The eddies in the surface layer are highly inhomogeneous in the vertical (z), but are clearly homogeneous in the horizontal direction. The LES attempts to resolve to the order of the grid scale, the energy-containing eddy structures.

Using a grid filter, one can split the fluctuating instantaneous velocity and potential temperature into resolved and subfilter-scale (SFS) components. The canonical, quasi-stationary equilibrium ABL is driven from above by the horizontal mesoscale geostrophic wind velocity vector $\boldsymbol{u}_g$, and the Coriolis force is converted into a mean horizontal pressure gradient oriented perpendicular to $\boldsymbol{u}_g$. In the LES of ABL, the molecular viscous forces are neglected and the surface roughness elements of scale z_0 are not resolved by the first grid cell ($z_0 \ll \Delta z$). Buoyancy forces are accurately predicted using the Boussinesq approximation. The momentum equation for resolved velocity contains an SFS stress tensor that is modeled using an eddy-viscosity formulation with the velocity scale being generated through a one-equation formulation for the SFS turbulent kinetic energy [36,37]. The LES equations are shown as follows in Eqs. (1–3). A detailed discussion of the numerical methods is available in [38–40]. In Eq. (1), $\tilde{\boldsymbol{u}}$ represents the filtered velocity, τ^{SFS} the SFS stresses, p^* the modified pressure, and $\tilde{\theta}$ the filtered potential temperature:

$$\nabla \cdot \tilde{\boldsymbol{u}} = 0 \tag{1}$$

$$\frac{\partial \tilde{\boldsymbol{u}}}{\partial t} + \nabla \cdot (\tilde{\boldsymbol{u}}\tilde{\boldsymbol{u}}) = -\nabla p^* - \nabla \cdot \tau_u^{\mathrm{SFS}} + \frac{g}{\theta_0}(\tilde{\theta} - \theta_0) + f \times (\boldsymbol{u}_g - \tilde{\boldsymbol{u}}) \tag{2}$$

$$\frac{\partial \tilde{\theta}}{\partial t} + \nabla \cdot (\tilde{\theta}\tilde{\boldsymbol{u}}) = -\nabla \cdot \tau_\theta^{\mathrm{SFS}} \tag{3}$$

Although the effects of buoyancy are highly pronounced in ABL turbulence and significantly impact its structure [39,40], we chose a more benign neutral stratification for this study. The domain size is restricted to $400 \times 400 \times 600$ m, which is sufficiently large to capture both the atmospheric scales as well as those relevant to small fixed wind unmanned vehicles. The Cartesian LES grid has a resolution of

$200 \times 200 \times 300$ m for a uniform spacing of 2 m in each spatial direction. To realistically mimic the interface between the mesoscale and microscale atmospheric turbulence, a capping inversion was specified at a height of 280 m. The surface heat flux is set to zero for this neutral ABL simulation, and a Coriolis parameter of $f = 0.0001$ s^{-1} is chosen to represent continental U.S.A. The bottom surface is modeled as uniformly rough with a characteristic roughness scale of 16 cm that is typical of grasslands. The dynamic system described in Eqs. (1–3) is forced by an imposed mean pressure gradient $\nabla\bar{P}$, usually specified in terms of a geostrophic wind as $\nabla\bar{P} = -f \times \boldsymbol{u}_g$. For this model, $\boldsymbol{u}_g$ magnitude is set to 8 m $\cdot$ s^{-1}, which corresponds to a moderately windy day. The equation system is solved using the pseudo-spectral method in the horizontal with periodic boundary conditions and second-order finite difference in the vertical. The time marching is accomplished using a third-order Runge–Kutta method. The computational setup is exactly as shown in Fig. 1. Further details about the computational methods and models can be obtained from [38–40].

2. *Validation of Results*

Large-eddy simulation is well established as a high-fidelity bench tool for modeling near-surface atmospheric flows. The fidelity of the modeling framework has been validated for equilibrium conditions using experimental data [41] and well-known phenomenology [38]. In this study, we adopt a similar strategy and assess the nondimensional near-wall scaling from simulation data with respect to the law of the wall, and Monin–Obukhov similarity theory arguments for neutral stratification. Particularly, we compute the nondimensional mean gradient $\Phi_M = (\kappa Z/u_\tau)d\langle\tilde{u}\rangle/\mathrm{d}z$, which should be closer to unity in the inertial logarithmic region of the ABL. The nondimensional mean gradient was obtained using the appropriate choice of near-surface parameters for length (distance from the wall z) and velocity (friction velocity u_τ). For a constant value of the mesoscale wind and surface heat flux, the turbulent flowfield evolves into a fully developed equilibrium boundary layer. After verifying the existence of statistical stationarity, converged statistics were estimated. Figure 2 shows the near-wall variation of Φ_M as a function of normalized distance from the surface (z/z_i), where z_i is the height of the ABL. We observe that Φ_M is nearly unity with small deviations arising from a combination of inaccuracies, including numerical errors and near-wall modeling [42]. The LES quality is considered acceptable as long as these deviations are small.

B. Reduced-Order Wind Representations

After obtaining wind data from the LES described earlier, a reduced-order representation of the ABL data can be constructed to assess the importance of the details of the wind field, and to reduce the memory requirements, proper orthogonal decomposition [43] is used.

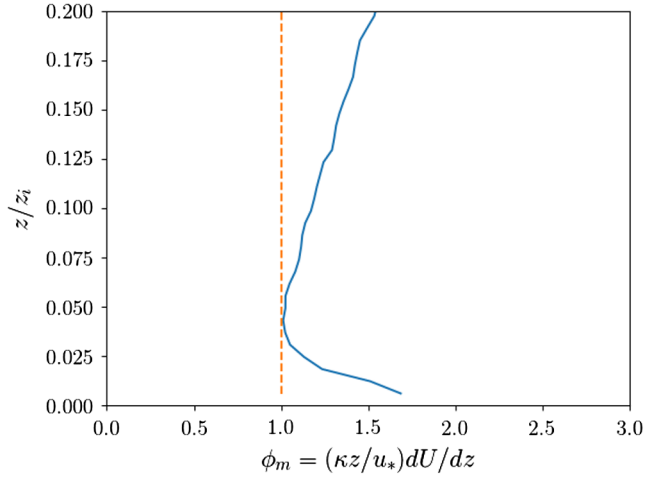

Fig. 2 Comparison of the nondimensional mean velocity gradients in the surface layer for neutral ABL with $\kappa = 0.4$.

Given a matrix A of size $m \times n$, the singular value decomposition is given by

$$A_{m\times n} = \hat{U}_{m\times n}\Sigma_{m\times m}V^*_{n\times n}$$

where $\hat{U}$, Σ, and V are matrices of the left singular basis vectors, singular values, and unitary right singular vectors, respectively. For every component of velocity, the data are stacked into a rectangular matrix. That is, each column represents time instances, and each row has the velocity in the three dimensions stacked as a column vector of length $Nx \times Ny \times Nz$.

The fraction of energy corresponding to each singular value, $\sigma^2(i)/\sum\sigma^2(i)$, is shown in Fig. 3.

A reduced-order representation can be constructed by using projections on a truncated number of modes $N < 100$. For the wind data, we have chosen N to be 10 modes, and we have reconstructed the new wind fields as will be presented in the Results section.

C. Benchmark Wind Model: Dryden Turbulence Model

Having LES wind data, one can determine mean wind velocities by temporally and spatially averaging the data. Once the mean wind is known (via simulation or experimental measurements), there are empirical models that estimate the velocity fluctuations, such as the Dryden model [31], which is a well-known benchmark wind model. The Dryden wind turbulence model uses an empirical spectral representation to add velocity fluctuations to the mean velocity. In this work, a continuous representation of the Dryden velocity spectra with positive vertical and negative lateral angular rates spectra is used. This representation is based on the Military Handbook MIL-HDBK-1797B [44]. The inputs to the Dryden model are altitude, vehicle velocity (in the inertial reference frame), and direction cosine matrix, and the output is the gust velocity in the body frame. The mean wind velocity is then added to the fluctuations to represent the full wind.

The current model provides the mean wind velocity using the U.S. Naval Research Laboratory Horizontal Wind Model routine. The typical inputs to this model are altitude, longitude, geopotential altitude, and the specific time of interest. The model predictions vary for different locations in the world and time of the year, and are of a very low fidelity compared with the ABL simulation. Thus, we have used the ABL data (Sec. II) to input the wind magnitude and direction for comparison purposes.

Data from sample atmospheric simulations are used to determine the magnitude of the wind velocity and the wind direction that are inputs to the aforementioned built-in MATLAB functions. Specifically, the mean wind speed and direction at 6 m are inputs to the Dryden wind turbulence model. Those values are approximately 3.40 m $\cdot$ s^{-1} and 240 deg, respectively. It is noted that the wind direction is measured from the north in a clockwise positive setting.

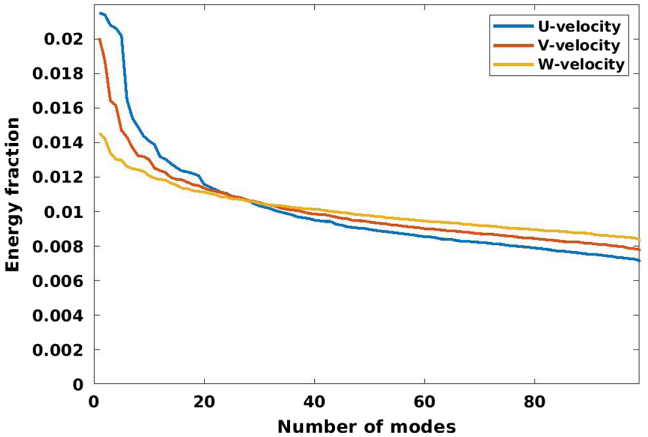

Fig. 3 Energy contained in each singular mode.

III. Aerodynamic Model

In this work, each rotor of a quad-copter is modeled individually using fundamental potential flow theory, while taking into account tools from helicopter rotor aerodynamic modeling. Blade element momentum theory (BEMT) was used in this paper as the rotor inflow ratio varies radially across the blade span. Also, the vehicle inflow dynamics at each time instant is treated as quasi-steady. Mishra et al. [45] utilized a BEMT model based on [46] for a fixed-wing aircraft. They validated their propeller thrust estimations against CFD simulation data. It is noted that rotors of a quad-copter in vertical flight experience the same condition of a propeller of a fixed-wing UAV in cruise flight. It is noted that the model used in this study still involves a high degree of simplification in forward flight. More advanced rotor aerodynamic models that consider in-plane inflow to the rotor disk (neglected in the current model) have the potential to improve the accuracy of the predictions. Such models may be replaced as an independent block without any further modifications required in the flight simulation package.

Blade element momentum theory uses and combines the two fundamental aerodynamic theories [46], namely, momentum and blade element theories. Momentum theory relates the thrust coefficient C_T to inflow velocity ratio where rotor is treated as a disk through which a flux of airflow passes. Hence, it does not process any information about the blade shape. On the other hand, the blade element theory uses blade geometric and aerodynamic characteristics, such as *chord length* and *twist* angle *distribution*. The blade element theory can be used to determine the thrust coefficient using strip theory to integrate lift over the blade span. The sectional lift coefficient C_l is determined by estimating the two-dimensional lift curve slope C_{l_α} and the pitch and inflow angles:

$$C_l = C_{l_\alpha}\alpha_{\text{eff}} \tag{4}$$

where $\alpha_{\text{eff}} = (\Theta + \alpha_{L=0} - \Phi)$ is the effective angle of attack, Φ is the inflow angle $(\lambda(r)/r)$, λ is the rotor inflow ratio, Θ is the blade pitch angle, $\alpha_{L=0}$ is the absolute value of the zero-lift angle of attack, and r represents the rotor radius.

The sectional lift for higher effective angles of attack can be represented by a poststall model [47]. That is, Eq. (4) can be replaced by Eq. (5):

$$\begin{aligned} C_l &= (1-\sigma)C_{l_\alpha}\alpha_{\text{eff}} \\ &\quad + \sigma[2\text{sign}(\alpha_{\text{eff}} - \alpha_{L=0})\sin^2(\alpha_{\text{eff}} - \alpha_{L=0})\cos(\alpha_{\text{eff}} - \alpha_{L=0})] \\ \sigma &= \frac{1 + e^{-M(\alpha_{\text{eff}} - \alpha_{L=0} - \alpha_0)} + e^{M(\alpha_{\text{eff}} - \alpha_{L=0} + \alpha_0)}}{[1 + e^{-M(\alpha_{\text{eff}} - \alpha_{L=0} - \alpha_0)}][1 + e^{-M(\alpha_{\text{eff}} - \alpha_{L=0} + \alpha_0)}]} \end{aligned} \tag{5}$$

where σ is the blending function, $\pm\alpha_0$ are the cutoffs, and M is the transition rate.

In BEMT [46], the rotor inflow ratio can be determined as a function of the flight condition parameters and geometric characteristics of the rotor by equating the thrust obtained from momentum and blade element theories. The following equation shows the resultant rotor inflow ratio:

$$\lambda(r) = \sqrt{\left(\frac{\sigma C_{l_\alpha}}{16F} - \frac{\lambda_c}{2}\right)^2 + \frac{\sigma C_{l_\alpha}}{8F}\Theta r} - \left(\frac{\sigma C_{l_\alpha}}{16F} - \frac{\lambda_c}{2}\right) \tag{6}$$

where F is given as

$$F = \frac{4}{\pi^2}\cos^{-1}(\exp(-f_{\text{root}}))\cos^{-1}(\exp(-f_{\text{tip}})) \tag{7}$$

where λ_c is the climb ratio; σ is the blade solidity; $f_{\text{root}} = (N_b/2)[r/(1-r)\Phi]$; $f_{\text{tip}} = (N_b/2)[(1-r)/r\Phi]$; the function F is Prandtl's tip loss function to compensate for the loss in lift near the tip and root of the blade, with Θ being the blade pitch; and N_b is the number of blades. Let $-V_{\text{rel}_{B_z}}$ denote the total inlet velocity, and let V_{tip} denote the blade tip velocity. In this study, λ_c is obtained as

$$\lambda_c = -\frac{V_{\text{rel}_{B_z}}}{V_{\text{tip}}} \tag{8}$$

Note that $V_{\text{rel}_{B_z}}$ denotes the projection of the relative wind velocity along the positive z direction of the body frame (i.e., positive inlet flow). The negative sign in $V_{\text{rel}_{B_z}}$ is required, because the positive sense of z is defined downward, and a positive λ_c implies climb for which the velocity in the body frame is negative. This model can be used in forward flight.

The total thrust of a rotor is obtained by integrating the sectional lift from hub ($R_{\text{min}} = 0.1R$ for the blade used in this study) to tip as follows:

$$T = N_b \int_{R_{\text{min}}}^{R} \frac{1}{2}\rho C_l[(r\omega)^2 + (\lambda V_{\text{tip}})^2]c(r)\ \mathrm{d}r \tag{9}$$

where $c(r)$ is the chord distribution from hub to tip. This model for a single rotor is compared with the experimental data of Ref. [48] in Fig. 4. The results correspond to a rotor with a radius of 7.62 cm, an average chord of 1.10 cm, and the twist distribution varying approximately from 25 to 5 deg from root to tip. It is noted that $C_{l_\alpha} = 1.7059\pi$ and $\alpha_{L=0} = 4$ deg.

As noted in Fig. 4, the thrust values predicted by the radial inflow model are in good agreement with the experimental data, whereas the torque values are underestimated. Torque values predicted by the performance model (that will be discussed next) only represent the resisting torque due to aerodynamics; however, additional frictional resistance in the shaft of the propeller may have manifested itself in the experimental torque data.

A. Torque and Power Performance Model

For a standard quad-copter (with a " +" rotor configuration shown in Fig. 5), the roll and pitch moments (τ_x and τ_y) are produced using differential thrust among the four rotors:

$$\tau_x = l(T_4 - T_2), \qquad \tau_y = l(T_1 - T_3) \tag{10}$$

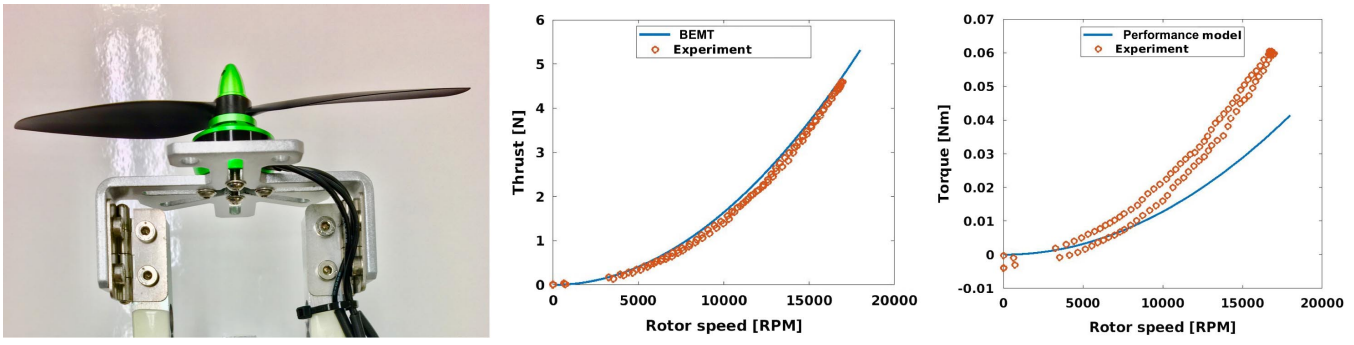

Fig. 4 Comparison between experimental data and the radial inflow model (BEMT) for hovering flight.

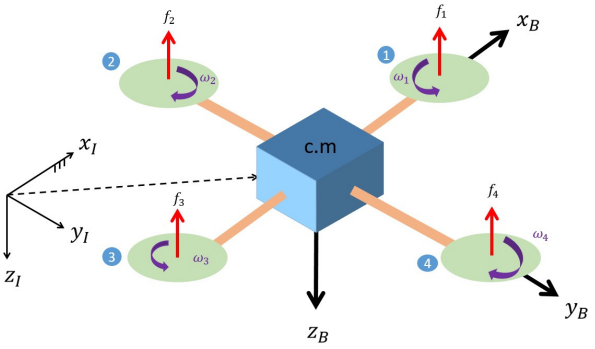

Fig. 5 Definition of the body and inertial frames of reference.

where l is the distance between the rotor and center of mass (c.m.). By modulating each rotor speed, it is possible to modify thrust and generate the required torque. The yaw moment τ_z is obtained by adding the reactive yaw moment of each rotor. The reactive moment for each rotor is a function of multiple aerodynamic contributors that will be discussed in detail next.

In forward flight, for a single rotor, the power required to overcome the resisting moment can be categorized as follows (in coefficient form, nondimensionalized by $\rho\pi R^5\omega^2$):

1) Induced power is the power that is used to overcome lift-induced drag, $C_{P,\text{ind}} = 1.15C_T^2/2\sqrt{\lambda^2+\mu^2}$, in which the advance ratio is defined as $\mu = \sqrt{V_{\text{rel}_{B_x}}^2 + V_{\text{rel}_{B_y}}^2}/V_{\text{tip}}$.

2) Blade profile power is the power required to overcome the viscous drag of each blade, $C_{P,0} = (\sigma C_{d0}/8)(1+4.6\mu^2)$, where C_{d0} is the profile drag coefficient ($C_{d0} = 0.008$).

3) Parasite power is the power required to overcome the drag exerted on the body of the vehicle due to the incoming freestream, $C_{P,p} = (1/2)(f/A)\mu^3$. It is noted that, for a rotor of a quad-copter, a 1/4 factor should be multiplied to $C_{P,p}$. The variable f is the equivalent flat-plate area that models the body of the vehicle; f/A can be approximated to be 1.

4) Climb or descent power is the power required/produced in climbing/descending flight, $C_{P,c} = C_W\lambda_c$.

Therefore, the total power required is

$$C_P = \frac{1.15C_T^2}{2\sqrt{\lambda_0^2+\mu^2}} + \frac{\sigma C_{d0}}{8}(1+4.6\mu^2) + \frac{1}{8}\frac{f}{A}\mu^3 + C_W\lambda_c \tag{11}$$

The power and torque coefficients are the same ($C_P = C_Q$). Thus, given Eq. (11), one can express the yaw torque due to the ith rotor as $Q_i = C_P\rho\pi R^5\omega_i^2$. Thus, the total reactive torque can be written as

$$\tau_z = \sum_{i=1}^{4} Q_i(\text{sign}(\omega)) \tag{12}$$

The term sign(ω) is required to make sure that the torque value associated with each rotor is taken into account with its correct sign, where counterclockwise rotation direction provides a positive reaction torque (for instance, see rotor 1 in Fig. 5). For yaw control, it is possible to mount the rotors with a small cant angle to improve the yaw authority of the platform with negligible reduction in vertical thrust. This is a desired configuration, in particular, when high-revolutions-per-minute low-torque motors are used.

B. Lumped Drag Model

The total drag on a quad-copter involves combinations of different aerodynamic effects, some of the contributions to which were discussed previously in the context of the required torque/power to turn the four rotors at the desired speed given a flight condition. It is noted that one physical phenomenon can lead to both additional required power and drag force on the quad-copter. The prominent contributors to the drag of a quad-copter are induced drag, blade profile drag, and translational drag due to the swirl of the induced velocity in forward flight. Parasite drag is typically small relative to the other contributors.

These parameters were studied in [49], and a lumped drag model for a quad-copter was introduced in Eq. (13) that related the drag (defined in the body frame) to thrust value and relative velocity seen by the quad-copter:

$$\boldsymbol{D} = -\begin{bmatrix} \bar{c}_d & 0 & 0 \\ 0 & \bar{c}_d & 0 \\ 0 & 0 & 0 \end{bmatrix} T\boldsymbol{V}_{\text{rel}_B} \tag{13}$$

where $\bar{c}_d$ is the lumped drag coefficient that was inferred from measured onboard accelerometer data for a typical quad-copter; $\bar{c} = 0.04 \pm 0.0035$. In this study, $\bar{c} = 0.04$ is used. Drag in the inertial frame is in the direction of the incoming velocity, whereas Eq. (13) represents rotor in-plane force that has no component in the z direction of the body-frame coordinate system.

In general, several interactions exist between the rotor blades and the wake, and between the rotor and airframe. Ventura Diaz and Yoon [22] performed high-fidelity CFD simulations and suggested that the airframe can reduce rotor–rotor interaction, and hence, increase the total thrust. With the requirement for the models to be near real time, the aerodynamics of each rotor is treated individually and rotor–rotor interaction effects are not considered in this study.

IV. Vehicle Dynamic Model and Control Hierarchy

The schematic of the vehicle and frames of references is given in Fig. 5. The body frame $B = \{x_B, y_B, z_B\}$ is needed to describe the orientation of the vehicle with respect to the inertial frame, whereas the inertial frame $I = \{x_I, y_I, z_I\}$ is used to locate the position of the c.m. of the vehicle. The modulation of the voltage to the electrical motor of each rotor modifies the angular velocity of each propeller ω_i ($i = 1, \ldots, 4$), which in turn governs both the rotational and translational dynamics due to the generated forces f_i ($i = 1, \ldots, 4$). The angular velocities are paired, that is, the first and third rotors rotate in a counterclockwise manner, whereas the second and fourth rotors rotate in a clockwise manner, such that the net torque around the body z axis due to the rotation of propellers is zero during hovering flight.

Equations of motion can be derived using the Newton–Euler method that uses the transport theorem [50]. The overall control of the vehicle is achieved through the combination of position control and attitude control. Figure 6 depicts a typical outer/inner control loop strategy along with the interconnection of the main components of an algorithm for control purposes. Let $\boldsymbol{r} \in \mathbb{R}^3$ and $\boldsymbol{v} \in \mathbb{R}^3$ denote the position and velocity vectors of the c.m. of the quad-copter, respectively, in the inertial coordinate system, and let $[\phi, \theta, \psi]^T$ denote the orientation angles in a standard (roll–pitch–yaw) 3–2–1 Euler rotation sequence. Let $\boldsymbol{\Omega} = [p, q, r]^T$ denote the components of the angular velocity vector of the body frame relative to the inertial frame when expressed in the body frame—the so-called body rates. Our goal is to derive control commands, namely, thrust control T and control torque $\boldsymbol{\tau}_B$ to follow a nominal trajectory.

The nominal trajectory is usually generated in an off-line fashion through a path planner (or guidance algorithm) [17]. The "navigation" block represents any navigation algorithm. The outputs of the "path planner" block are the desired time histories of the states of the system that have to be tracked. In Fig. 6, the position, velocity, body rates, and heading angle are shown to be the outputs of the guidance block. (The subscript c is used to specify these values as commanded values that have to be tracked.) These values are fed to the "controller" block. At this stage, the position controller is used to track commanded values of position and velocity (i.e., $\boldsymbol{r}_c$ and $\boldsymbol{v}_c$). This task is achieved through a second-order differential error-tracking equation as

$$\ddot{\boldsymbol{r}}_e + \boldsymbol{K}_d\dot{\boldsymbol{r}}_e + \boldsymbol{K}_p\boldsymbol{r}_e = \boldsymbol{0} \tag{14}$$

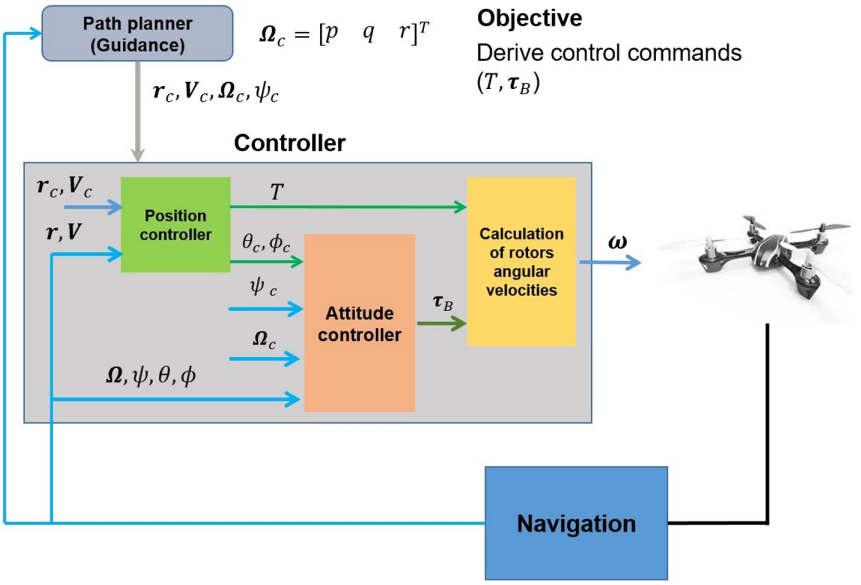

Fig. 6 Outer/inner control loop scheme for position and attitude control of a quad-copter.

where $\boldsymbol{r}_e = \boldsymbol{r}_c - \boldsymbol{r}$ denotes the position error, and $\boldsymbol{K}_d$ and $\boldsymbol{K}_p$ are positive definite gain matrices to ensure acceptable time characteristics of a second-order response. A virtual control vector $\boldsymbol{U}$ is defined as

$$\boldsymbol{U} = \ddot{\boldsymbol{r}} = \ddot{\boldsymbol{r}}_c + \boldsymbol{K}_d(\boldsymbol{v}_c - \boldsymbol{v}) + \boldsymbol{K}_p(\boldsymbol{r}_c - \boldsymbol{r}) \tag{15}$$

Following Ref. [51], this virtual control input can be used along with the translational and rotational equations of motion to compute the desired thrust T, roll angle ϕ_c, and pitch angle θ_c. Thus, if these three variables are tracked to a good degree of accuracy, one has essentially realized the position and velocity vectors that are commanded by the path-planning algorithm. The two angles, θ_c and ϕ_c, along with the commanded yaw altitude ψ_c and the commanded body rates $\boldsymbol{\Omega}_c$ (computed through a tracking differentiator [51]), constitute the input data to the inner loop (attitude controller).

The goal of the attitude controller is to track the intermediate commanded values (i.e., those that are the outputs of the position controller) and those values that are commanded by the path-planning block. The output of the attitude controller is, therefore, the control torque vector $\boldsymbol{\tau}_B$, which will result in accurate tracking of Euler angles and body rates. Eventually, the thrust and torque vectors are used to compute rotor angular velocity vector $\boldsymbol{\omega} = [\omega_1, \omega_2, \omega_3, \omega_4]^T$. The details of the algorithms can be found in Ref. [51].

V. Aerodynamic Models and Coupling to Flight Dynamics

In this section, the coupling of two aerodynamic models, one of which is based on Sec. III, to the vehicle dynamics is described. Note that the resulting model is intended for fast (real-time or near real-time) trajectory prediction and validation applications.

A. Simplistic Performance Model

In this approach (also known as the static model), the thrust and torque of the ith rotor ($i = 1, \ldots, 4$) are modeled as quadratic functions of the rotor revolutions per minute for hovering fixed-pitch rotors:

$$Q_i = k\omega_i^2, \qquad T_i = b\omega_i^2 \tag{16}$$

where k and b are referred to as the effective torque and thrust coefficients, which can be determined experimentally, or using CFD analysis for a given rotor using simple quadratic curve fitting [52]. Using experimental data shown in Fig. 4, these coefficients are estimated to be equal to $b = 1.5652 \times 10^{-8}$ N/rpm^2 and $k = 2.0862 \times 10^{-10}$ (N · m)/rpm^2.

Given these relations, one can form the following linear system of equations to relate the rotor rotation rate to the required net thrust and torque. Considering Eq. (10), and the fact that the sum of the thrust of rotors is the net thrust, one can derive the following relation for the total thrust magnitude and torque inputs:

$$\begin{bmatrix} T \\ \tau_x \\ \tau_y \\ \tau_z \end{bmatrix} = \begin{bmatrix} b & b & b & b \\ 0 & -bl & 0 & bl \\ -bl & 0 & bl & 0 \\ -k & k & -k & k \end{bmatrix} \begin{bmatrix} \omega_1^2 \\ \omega_2^2 \\ \omega_3^2 \\ \omega_4^2 \end{bmatrix} \tag{17}$$

Therefore, by solving Eq. (17), one can determine the rotation rate of each rotor. However, it is noted that this model is insensitive to wind conditions as well as the vehicle dynamics.

B. Radial Inflow Model

The radial inflow model, as described in Sec. III, is strictly valid for axial flight. In this work, the incoming wind velocity is projected to the axis of rotor and the thrust is estimated using BEMT. The benefit of this model—in comparison with the simplistic model—is its sensitivity to the wind condition and vehicle dynamics. The inputs to this model are the required thrust and the velocity relative to the body of the quad-copter.

Implementing this model along with the torque model introduces additional complications. First, an inverse problem should be solved, because the desired thrust is now given as an input and revolutions per minute must be computed. At every time instant, this is performed via a simple optimization routine. Second, the yaw torque τ_z is no longer a function of the revolutions per minute, and in fact, is a complex function as described in Eq. (12). Thus, the set of equations to solve for ω_i are

$$T = \sum_{i=1}^{4} T_i(\omega_i), \quad \tau_x = l(T_4(\omega_4) - T_2(\omega_2)),$$
$$\tau_y = l(T_1(\omega_1) - T_3(\omega_3)), \quad \tau_z = \sum_{i=1}^{4} Q_i(\omega_i)(-1)^{i+1} \tag{18}$$

It is clear that, because ω_i is implicit in all of the equations, an analytical solution cannot be found. Note that we need to solve for ω_i ($i = 1, \ldots, 4$) at every time instant along the trajectory, which is a

nonlinear root-finding problem. One way to provide an approximate solution to these set of equations for every time step is as follows:

1) At a given time instant and a given flight condition, for every thrust T_i, solve the inverse problem to find ω_i and the resultant Q_i.

2) For each rotor, use the relations $T_i = b_i\omega_i^2$ and $Q_i = k_i\omega_i^2$ to estimate the local values of b_i and k_i for that specific rotor and flight condition.

3) Use Eq. (17), where the coefficient matrix is given by

$$\begin{bmatrix} b_1 & b_2 & b_3 & b_4 \\ 0 & -b_2 l & 0 & b_4 l \\ -b_1 l & 0 & 0 & b_4 l \\ -k_1 & k_2 & -k_3 & k_4 \end{bmatrix}$$

to find the final revolutions per minute.

4) Calculate the net thrust and torque using newly found revolutions per minute, and feed them back into the dynamic model.

It has to be noted that the radial inflow model serves as a template for general aerodynamic module that can be replaced by higher-fidelity models (such as a CFD model).

VI. Results and Discussion

A quad-copter with the following physical and geometric characteristics is considered: mass $m = 0.69$ kg, arm length $l = 0.225$ m, X moment of inertia $I_x = 0.0469$ kg $\cdot$ m^{-2}, Y moment of inertia $I_y = 0.0358$ kg $\cdot$ m^{-2}, Z moment of inertia $I_z = 0.0673$ kg $\cdot$ m^{-2}, and rotor moment of inertia $I_r = 3.357 \times 10^{-5}$ kg $\cdot$ m^{-2}. The rotor radius is $R = 0.0762$ m.

The aerodynamic models for the quad-copter and the wind models (Sec. II) were integrated with the control module in the Simulink environment of MATLAB. The entire simulation suite is open sourced for use by the community.[**] We have performed flight simulations for two representative nominal trajectories: 1) an ascent–straight–descent trajectory and 2) a circular trajectory.

A. Ascent–Straight–Descent Path

Let Δt_i denote the time interval of the ith segment of a multisegment trajectory. Figure 7 shows the schematic of an idealized rectangular path that consists of five segments: 1) taking off vertically to an altitude of 40 m (where the initial and final vertical velocities are zero) over a time interval of $\Delta t_1 = 10$ s, 2) accelerating from zero forward velocity to a cruise constant speed of 15 m $\cdot$ s^{-1} over a time interval of $\Delta t_2 = 12$ s, 3) continuing with the cruise speed for $\Delta t_3 = 30$ s, 4) decelerating from a forward velocity of 15 m $\cdot$ s^{-1} to zero over a time interval of $\Delta t_4 = 15$ s, and 5) descending over a time interval of $\Delta t_5 = 10$ s. As the quad-copter follows the trajectory, it is subject to the wind field described in Sec. II. For all segments (except for the cruise segment 3), a cubic polynomial is used to enforce the boundary conditions on x, y, and z positions and velocity coordinates [53]. It is noted that the planned trajectory information consists of the planned

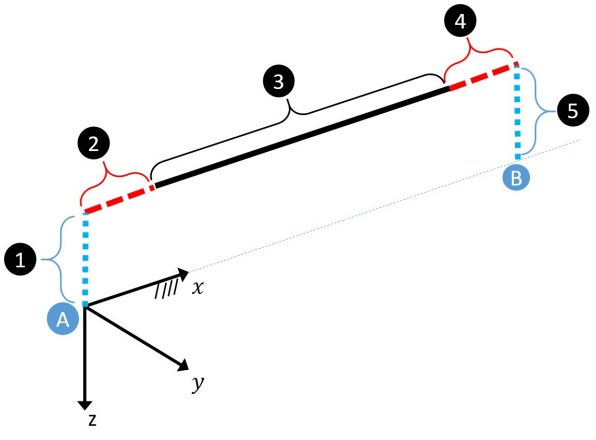

Fig. 7 Schematic of the ascent–straight–descent nominal trajectory.

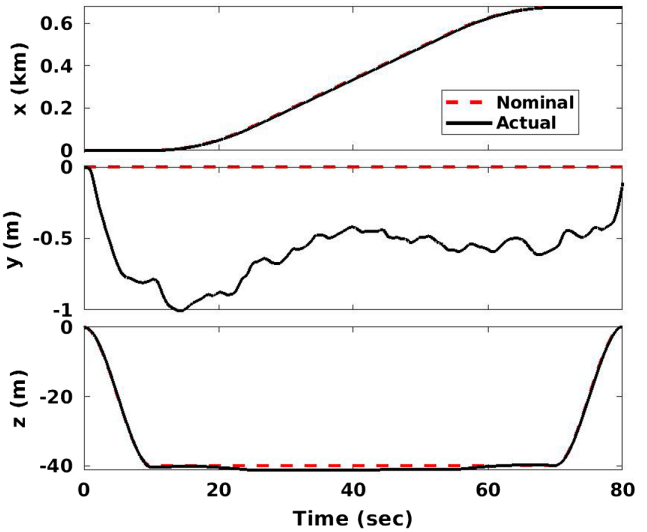

Fig. 8 Time histories of the inertial coordinates of the actual vs nominal trajectory.

position, velocities, and acceleration, as well as the heading (yaw) angle [$\psi(t) = 0$], all of which are used in the attitude controller block in Fig. 6. The results for different flight parameters are next presented using a full-wind representation and radial inflow model. The results demonstrate that the planned trajectory and the vehicle attitude and position are controlled successfully. The time histories of the quad-copter position and velocity coordinates as well as its attitude are shown in Figs. 8–10. All of the resultant flight parameters (shown in red dashed line) are compared with their planned ones (shown in black sold line). The resultant position vs planned position is shown in Fig. 8.

As noted, the quad-copter has tracked the planned trajectory with acceptable accuracy. The off-the-track y-position coordinate appears to have the largest deviation due to the side-wind effects. The planned and resultant velocities in the body frame are shown in Fig. 10, which reveals the fluctuations due to turbulent gusts.

The wind velocity at the vehicle c.m. is shown in Fig. 10, illustrating a desirable forward wind and an undesirable side wind experienced by the vehicle. The controller was able to handle wind fluctuation amplitudes of 0.4 m $\cdot$ s^{-1} in the X direction and 0.7 m $\cdot$ s^{-1} in the Y direction.

The Euler angles (ψ, θ, ϕ), body rates (p, q, r), and generated torques (τ_x, τ_y, τ_z) on the body of the quad-copter are shown in Fig. 11. As noted, the pitch angle is about $\theta = -20$ deg (pitch down) during the cruise phase of the flight (25 s $< t <$ 55 s).

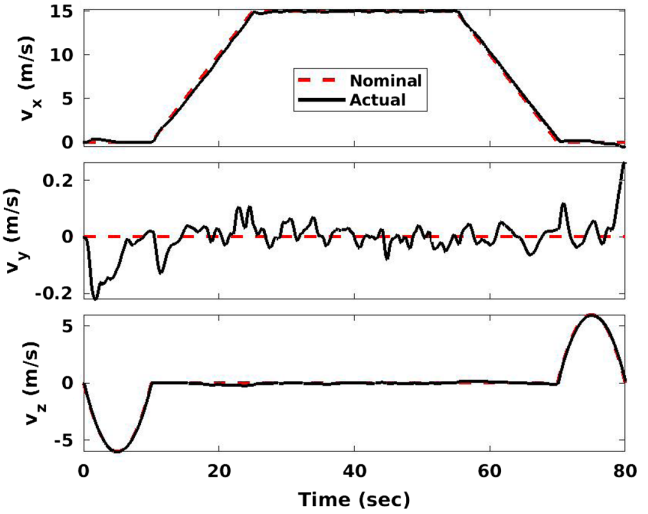

Fig. 9 Time histories of the inertial velocity of the quad-copter vs the nominal velocity.

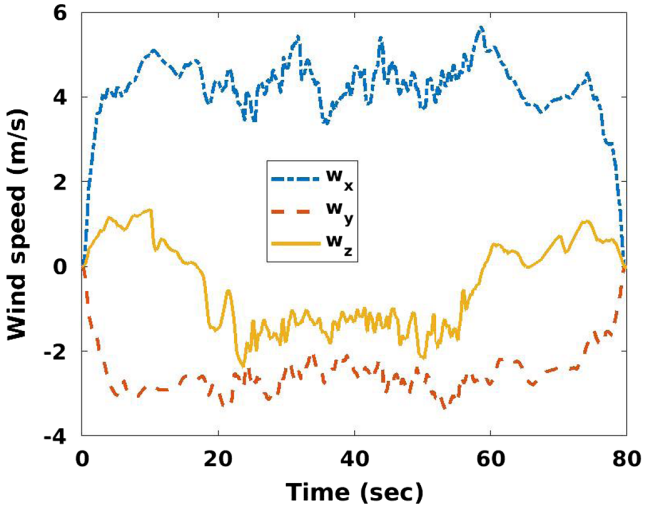

Fig. 10 Components of the wind velocity (in inertial frame) along the actual trajectory.

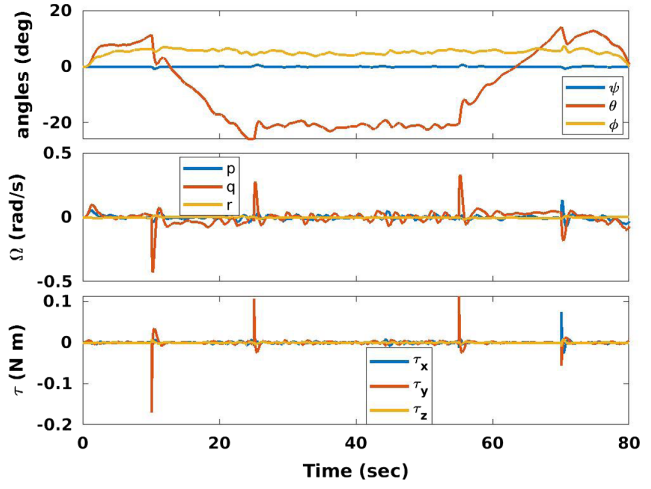

Fig. 11 Time histories of the Euler angles, body rates, and control torques.

The required rotor revolutions per minute to track the planned path are obtained using the radial inflow model and shown in Fig. 12. It is noted that the advance ratio is relatively low ($\mu = 0.12$) during the cruise phase.

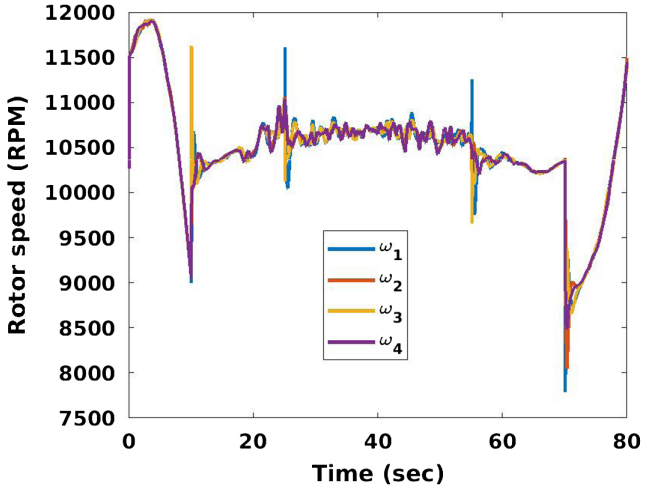

Fig. 12 Time histories of the rotor revolutions per minute along the trajectory.

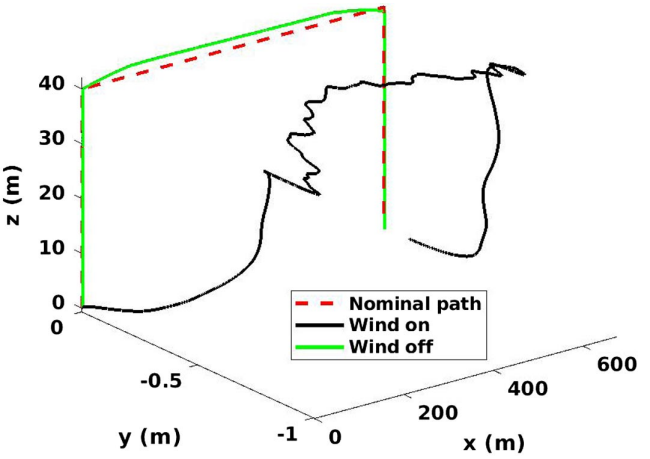

Fig. 13 Flown trajectories with and without consideration of wind (each axis is scaled differently for clarity).

The effects of the wind on the resultant trajectory and vehicle dynamics are shown in Figs. 13 and 14. It is noted that, without a wind field, the planned path was tracked with almost no deviations. It is also evident that wind effects on the revolutions per minute inputs are more prominent in the cruise section compared with the vertical takeoff and landing segments.

The difference between the simplified and radial inflow models in terms of the predicted rotor speeds is compared in Fig. 15. Note that the resultant revolutions per minute of only rotor 1 (leading rotor; see Fig. 5) in a no-wind condition is presented for clarity in depicting the discrepancy. The predicted revolutions per minute conditions (approximately 10,150) from both models are very similar in the hover case ($t = 10$ s and $t = 70$ s), as shown in Fig. 15. Also, during the takeoff and landing phases ($t < 10$ s and $t > 70$ s), both models provide closer rotor speed predictions. There is, however, a large discrepancy in the cruise section of the trajectory ($10 < t < 70$ s), where the velocity relative to the body of the quad-copter increases the inflow λ [see Eq. (6)]. Therefore, the lift coefficient [Eq. (4)] decreases because Φ increases. Hence, the rotor speed has to increase to maintain the required thrust.

The torque and power performance models, introduced in Sec. III.A, can be used to provide an estimate of the total required power during flight. Considering Eq. (11), one can simply write the total power as

$$P = \sum_{i=1}^{4} C_{P_i} \rho \pi R^5 \omega_i^3 \tag{19}$$

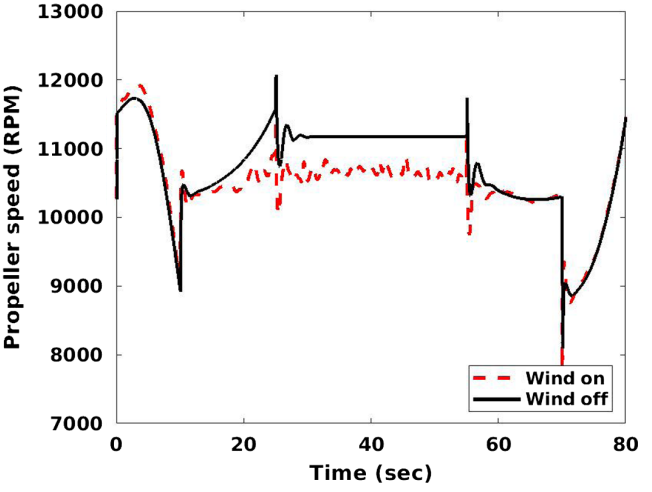

Fig. 14 Comparison of the rotor 1 rpm with and without consideration of wind.

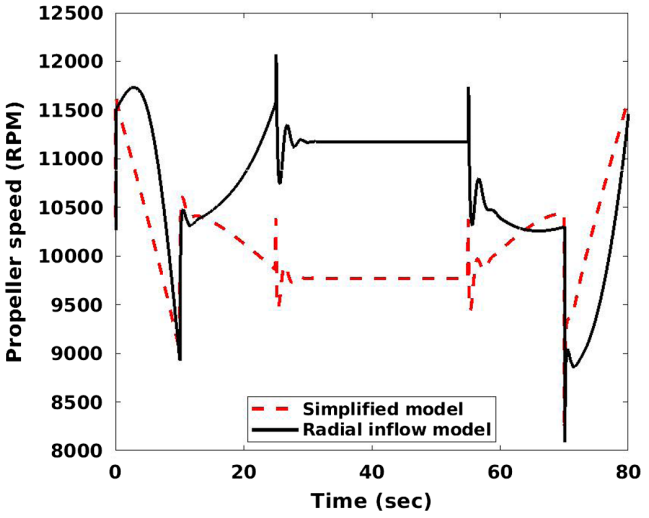

Fig. 15 Rotor revolutions per minute prediction with different models.

For the simplified model, the power estimate is simply $\sum_{i=1}^{4} k\omega_i^3$, where the value of k is obtained from the torque data of Fig. 4. The time history of the power estimated by both models is shown in Fig. 16.

The simplified model yields larger power values, and this is mainly due to the offset seen between the torque predictions of performance model and experimental data in Fig. 4. It is also apparent that takeoff ($t < 10$ s) requires more power than landing ($t > 70$ s). The radial inflow model represents this effect, whereas the simplified model is unable to do this.

To assess the importance of the wind model, the wind field is reconstructed using different numbers of modes, and flight simulations are performed to illustrate the impact on the results. A comparison between the resultant trajectories of the full-wind and reduced-order versions of the wind field, and the Dryden wind turbulence model is shown in Fig. 17. In these simulations, the radial inflow model was used as the aerodynamic model to compare the impact of the different wind models. The controller attempts to keep the quad-copter on the nominal path regardless of the wind model used. It is clear that the Dryden model, in which the fluctuations are not spatiotemporally correlated, results in a lesser deviation from the nominal trajectory. It is noted that fluctuations are spatiotemporally correlated in the LES model.

The incoming velocities in the three directions seen by the quad-copter for different wind models are shown as a function of time in Fig. 18.

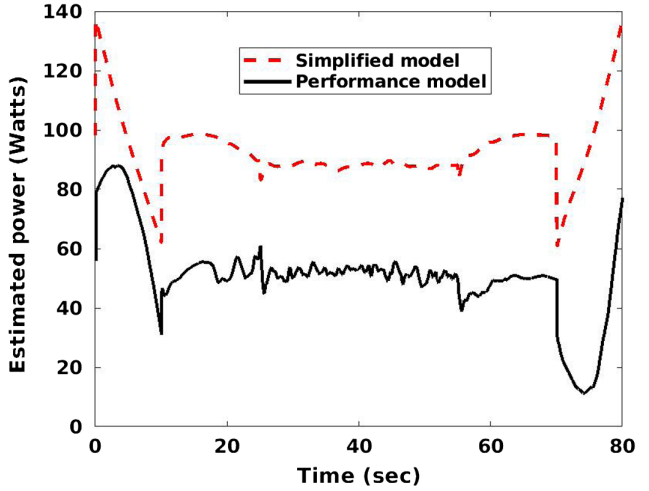

Fig. 16 Time histories of the required power estimates using different models.

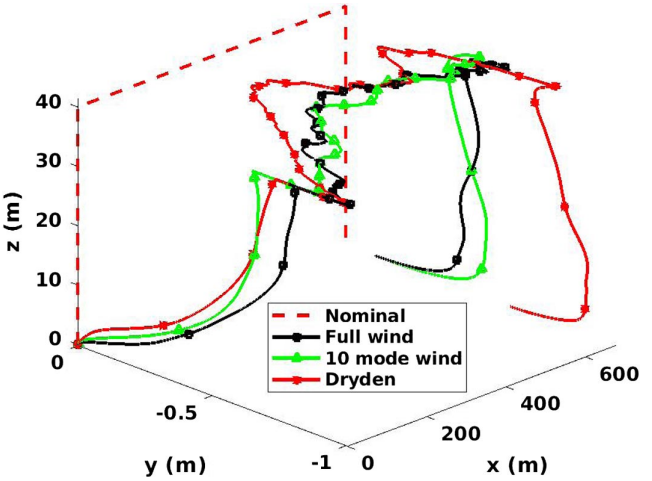

Fig. 17 Effect of different versions of wind model on the resultant trajectory.

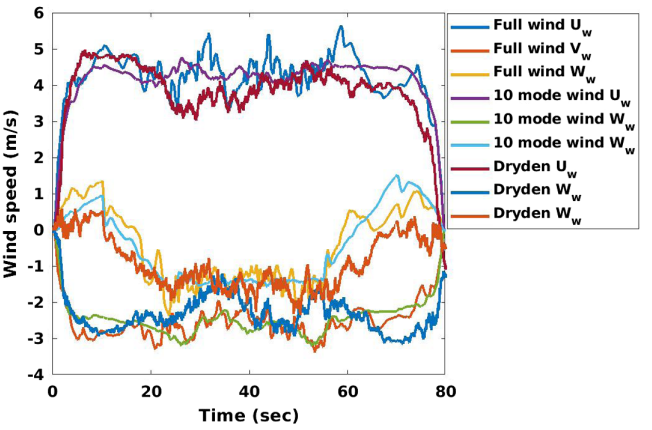

Fig. 18 Wind-velocity components in the inertial frame.

B. Circular Path

Flying in a circular path further accentuates the importance of the flight controller and wind model. In this case, the quad-copter has to follow a path with continuous acceleration. The presence of wind has both favorable and unfavorable effects during portions of the trajectory, as discussed herein. A schematic of the circular path and the wind condition is shown in Fig. 19.

Similar to the straight path, the trajectory for the circular path consists of five segments: 1) taking off to an altitude of 60 m, 2) accelerating for 10 s to a nominal speed while being in the circular path with radius of 80 m, 3) following the circular path with a nominal speed, 4) decelerating for 10 s to stop at the point where the circular path was initially started, and 5) landing.

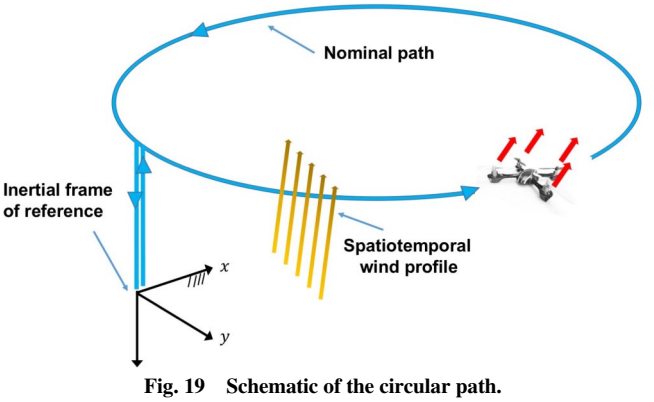

Fig. 19 Schematic of the circular path.

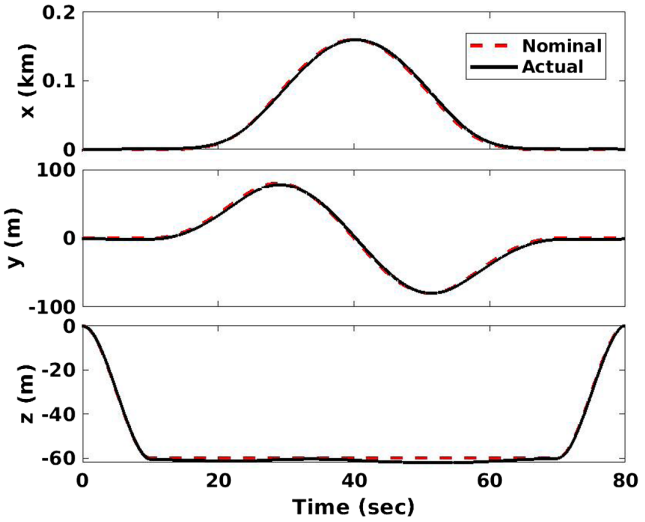

Fig. 20 Time histories of the position coordinates of the c.m. of the quad-copter for circular path.

A comparison between the planned and obtained locations and velocities in the three directions is shown in Figs. 20 and 21. The results are indicative of the fact that the vehicle has been able to track the planned path well and maintain the quad-copter on the nominal path.

The wind velocity at the c.m. of the quad-copter is shown in Fig. 22. The values are slightly larger compared with the straight path (see Fig. 10), given that the circular path has a higher altitude.

For this path, the commanded heading angle ψ_c was set to zero, which means the quad-copter does not turn around its Z axis, and the circular path was tracked by controlling only the roll and pitch angles. The Euler angles and their rated and resultant torques are depicted in Fig. 23.

As noted from Fig. 23, for the takeoff phase ($t < 10$ s), the quad-copter has to roll (right rotor 3 down) and pitch up (front rotor 1 up) to negate the incoming wind from the south west, and then continue the entire path with a nose-up position to negate the effect of the wind. The corresponding four rotor speeds shown in Fig. 24 were obtained as the controller commands computed to maintain the planned circular trajectory.

The actual vs planned trajectories are demonstrated for the circular path in Fig. 25. As expected, the actual trajectory is shifted toward positive x and negative y due to the wind condition. A maximum deviation of 2 m between the two paths is noted. The estimates of the required power obtained from the simplified and radial inflow models are shown in Fig. 26.

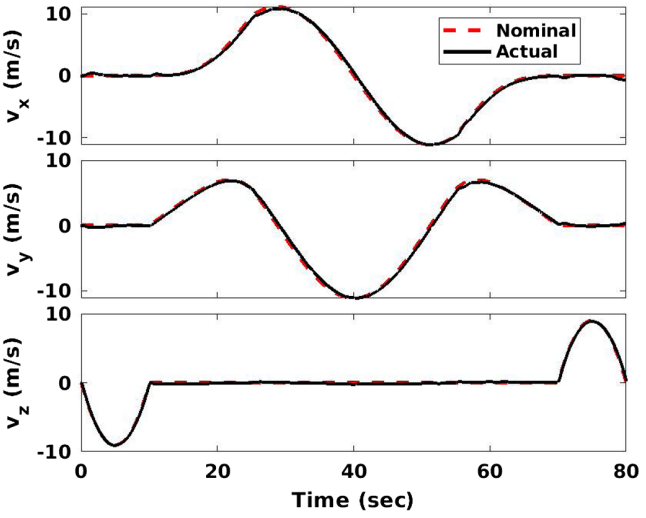

Fig. 21 Time histories of velocity coordinates of the c.m. of the quad-copter for circular path.

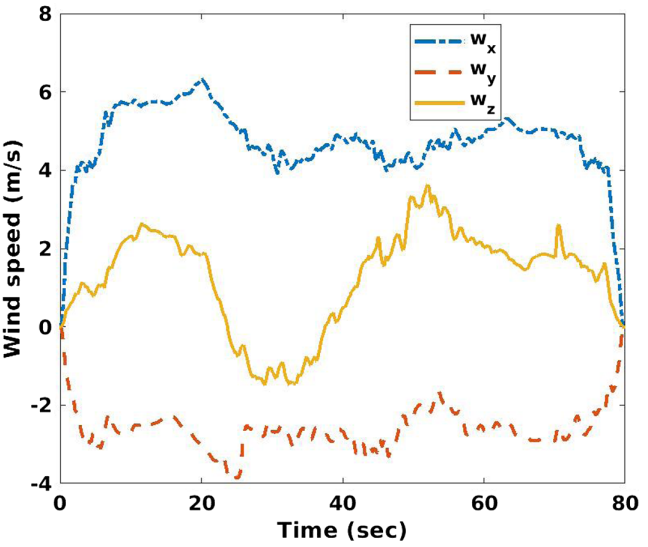

Fig. 22 Wind velocity at the c.m. of the quad-copter.

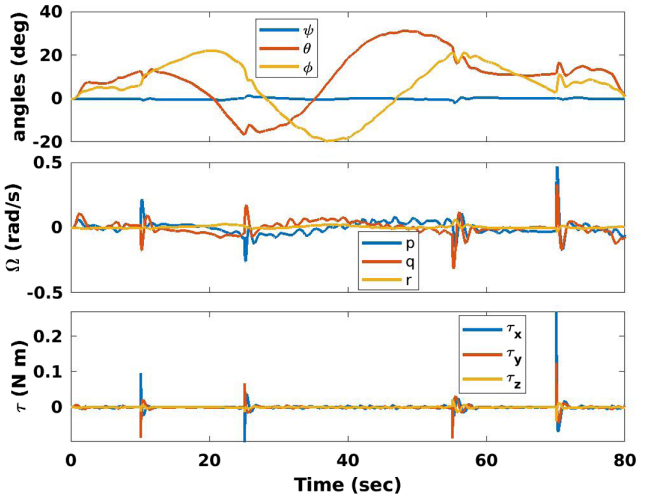

Fig. 23 Euler angles, body rates, and torques applied to the quad-copter during circular path.

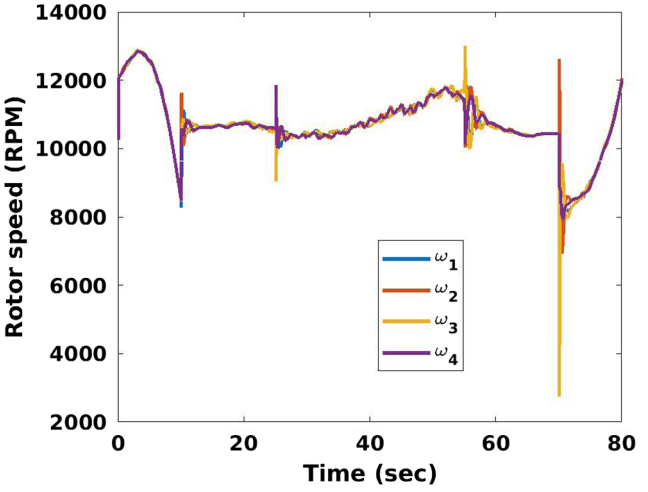

Fig. 24 Rotor speeds to maintain the quad-copter on the circular path.

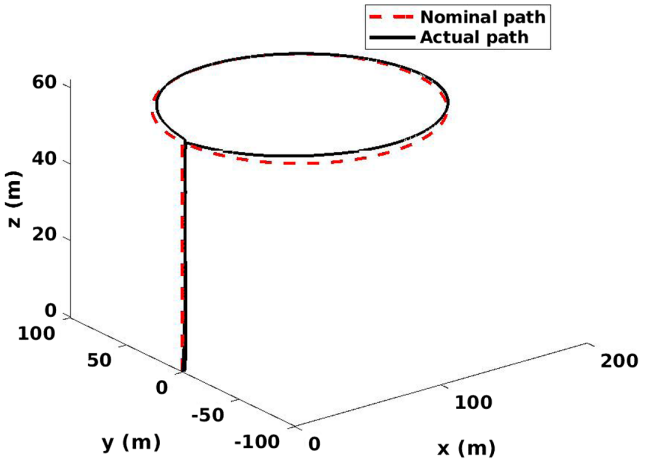

Fig. 25 Trajectories with and without consideration of wind for the circular path.

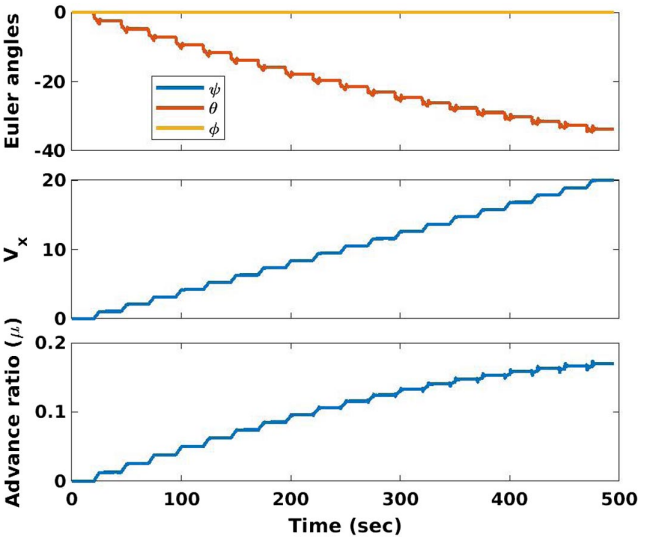

Fig. 27 Euler angles and cruise speed for optimal cruise speed determination.

When the quad-copter is on the circular trajectory ($10 < t < 70$ s), the simplified model shows a higher sensitivity to the favorable and adverse wind conditions. In the first half-circle ($10 < t < 40$ s), the wind is overall favorable. In the second half-circle ($40 < t < 70$ s), the wind causes unfavorable drag as well as more induced inflow to the rotors that leads to higher revolutions per minute (see Fig. 24), and subsequently, higher power, as depicted in Fig. 26.

C. Optimal Cruise Speed

The relationship between power and cruise speed is nonmonotone and nonlinear. The power model [see Eq. (11)] can be further analyzed to determine the optimal cruise speed and compared with the power required in hover. A new trajectory was defined, in which the quad-copter starts from hover, and the forward speed is adjusted incrementally on a straight path. Within each increment, it accelerates for 5 s to add 1 $\text{m} \cdot \text{s}^{-1}$ to its speed during the acceleration phase, and stays on that specific cruise speed for 20 s. This increment is performed 20 times, and the vehicle will eventually reach a forward speed of 20 $\text{m} \cdot \text{s}^{-1}$ in a total time of 500 s. The Euler angles and forward velocity in the inertial reference frame, and the advance ratio are shown in Fig. 27.

It is noted that the advance ratio μ is relatively small for the entire flight. At the highest forward speed of 20 $\text{m} \cdot \text{s}^{-1}$, the advance ratio is $\mu = 0.17$. The pitch angle increases in magnitude during the acceleration phase and maintains the same level during the constant cruise speed part of each increment. The speed of the quad-copter as a function of the leading rotor 1 (see Fig. 5) rotational speed is shown in Fig. 28.

As noted from Fig. 28, the power curve with the performance model [see Eq. (11)] has a local minimum around $V_x = 7.2$ $\text{m} \cdot \text{s}^{-1}$ (indicated with the green dashed line). It is also noted that the simplified model that only uses the rotor speed to estimate the power ($P = k \sum_{i=1}^{4} \omega_i^3$) estimates less power consumption for higher speeds. This is due to the fact that, at higher speeds, the drag [that is defined in the body frame; see Eq. (13)] provides an upward component when the pitch angle is negative ($\theta < 0$), thus augmenting the net vertical force. Therefore, the thrust required by the rotor (to sustain the altitude) decreases, and based on the simplified model, the required revolutions per minute should also decrease. The estimated revolutions per minute values of rotor 1 vs the forward speed from both models are shown in Fig. 29.

As expected, the two models show opposite trends. Based on Figs. 28 and 29, higher revolutions per minute does not necessarily indicate higher required power, as the flight condition has a significant impact on the total power.

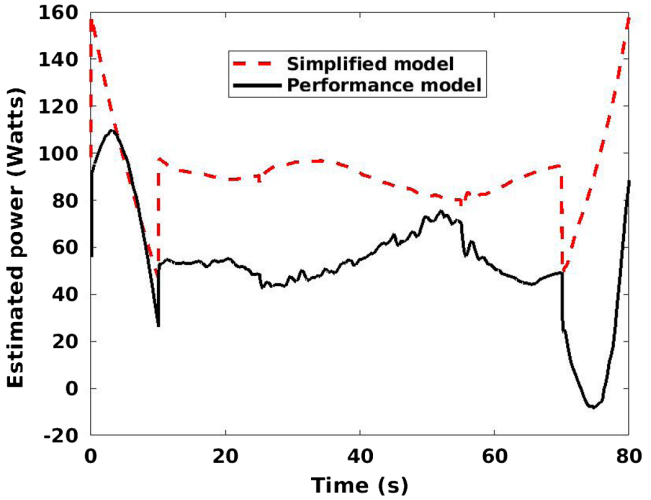

Fig. 26 Estimated required power through different models for circular path.

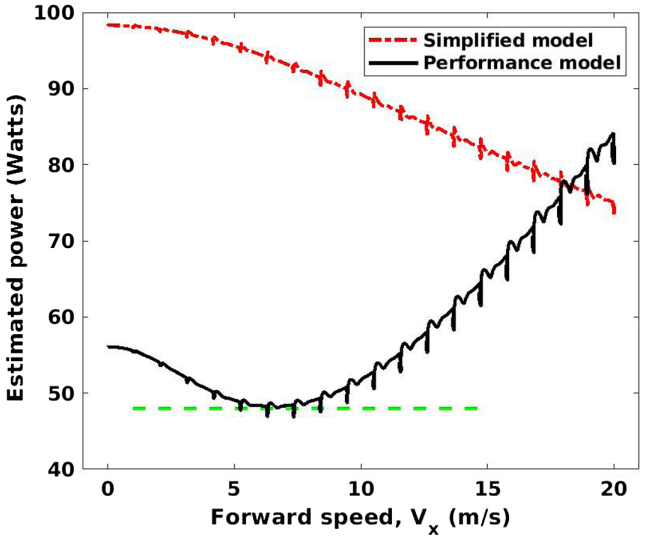

Fig. 28 Estimated required power vs cruise speed for simplified and radial inflow models.

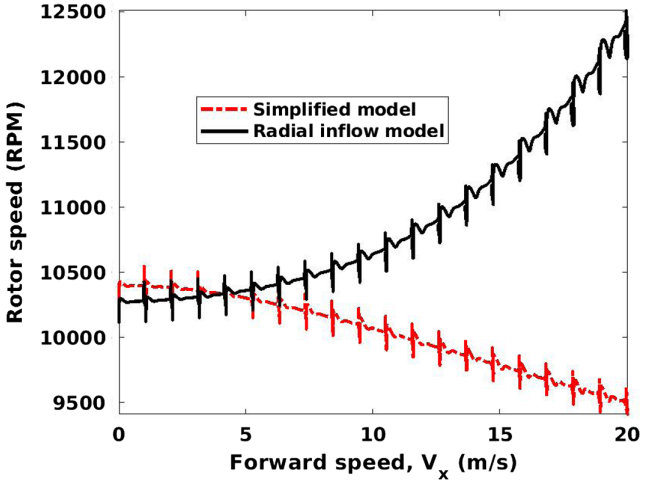

Fig. 29 Estimated rotor 1 speed as a function of cruise speed.

VII. Conclusions

A comprehensive suite of tools was introduced for performing realistic flight simulations for unmanned quad-copters. The focus is on operations in low-altitude atmospheric conditions, where turbulent gusts are expected to have a significant impact on the performance and stability of small unmanned aerial vehicles.

Large-eddy simulations were performed to accurately represent the ABL. The canonical ABL used to generate the data in this study is modeled as a rough flat wall boundary layer with surface heating from solar radiation, forced by a geostrophic wind in the horizontal plane, and solved in the rotational frame of reference fixed to Earth's surface. From the LES data, a reduced-order representation of the wind field was also constructed. Additionally, the Dryden turbulence model for wind velocity fluctuations was included as a benchmark wind model.

The aerodynamics of the quad-copter was modeled using adaptations of the BEMT. Models for thrust, drag, and power of the quad-copter were integrated with the flight dynamics and wind models. A nonlinear flight controller (backstepping controller) was developed to control all six DOF of the motion of the quad-copters.

An ascent–straight–descent path and a circular path were designed for the simulations of the closed-loop system. These two trajectories were of interest due to the fact that they both incorporate a representative set of possible trajectories of a quad-copter. Representative results for flight parameters, required revolutions per minute inputs, resultant trajectory and power of the quad-copter for different aerodynamic and wind models, and planned trajectories were obtained and compared against each other. A multiple cruise-speed trajectory phase was defined to determine the optimal cruise speed of the quad-copter.

Collectively, this study presented a new suite of tools for realistic flight simulations, and provides insight into the impact of modeling fidelity on trajectory planning and control. The entire simulation suite is open sourced for use by the community (See footnote **).

Acknowledgment

This work was supported by NASA under the project Generalized Trajectory Modeling and Prediction for Unmanned Aircraft Systems (technical monitor: Sarah D'Souza).

References

[1] Cai, G., Dias, J., and Seneviratne, L., "A Survey of Small-Scale Unmanned Aerial Vehicles: Recent Advances and Future Development Trends," *Unmanned Systems*, Vol. 2, No. 2, 2014, pp. 175–199. https://doi.org/10.1142/S2301385014300017

[2] Wall, T., and Monahan, T., "Surveillance and Violence from Afar: The Politics of Drones and Liminal Security-Scapes," *Theoretical Criminology*, Vol. 15, No. 3, 2011, pp. 239–254. https://doi.org/10.1177/1362480610396650

[3] Irizarry, J., Gheisari, M., and Walker, B. N., "Usability Assessment of Drone Technology as Safety Inspection Tools," *Journal of Information Technology in Construction (ITcon)*, Vol. 17, No. 12, 2012, pp. 194–212.

[4] Nex, F., and Remondino, F., "UAV for 3D Mapping Applications: A Review," *Applied Geomatics*, Vol. 6, No. 1, 2014, pp. 1–15. https://doi.org/10.1007/s12518-013-0120-x

[5] Zhang, C., and Kovacs, J. M., "The Application of Small Unmanned Aerial Systems for Precision Agriculture: A Review," *Precision Agriculture*, Vol. 13, No. 6, 2012, pp. 693–712. https://doi.org/10.1007/s11119-012-9274-5

[6] Gavrilovic, N., Benard, E., Pastor, P., and Moschetta, J.-M., "Performance Improvement of Small Unmanned Aerial Vehicles Through Gust Energy Harvesting," *Journal of Aircraft*, Vol. 55, No. 2, 2018, pp. 741–754. https://doi.org/10.2514/1.C034531

[7] Katz, J., "Aerodynamic Aspects of Unmanned Aerial Vehicle Aerial Refueling," *Journal of Aircraft*, Vol. 54, No. 6, 2017, pp. 2311–2316. https://doi.org/10.2514/1.C034373

[8] Niemiec, R., and Gandhi, F., "Multirotor Controls, Trim, and Autonomous Flight Dynamics of Plus- and Cross-Quadcopters," *Journal of Aircraft*, Vol. 54, No. 5, 2017, pp. 1910–1920. https://doi.org/10.2514/1.C034165

[9] Watkins, S., Milbank, J., Loxton, B. J., and Melbourne, W. H., "Atmospheric Winds and Their Implications for Microair Vehicles," *AIAA Journal*, Vol. 44, No. 11, 2006, pp. 2591–2600. https://doi.org/10.2514/1.22670

[10] Luo, J., Zhu, L., and Yan, G., "Novel Quadrotor Forward-Flight Model Based on Wake Interference," *AIAA Journal*, Vol. 53, No. 12, 2015, pp. 3522–3533. https://doi.org/10.2514/1.J053011

[11] Bannwarth, J. X., Chen, Z. J., Stol, K. A., MacDonald, B. A., and Richards, P. J., "Aerodynamic Force Modeling of Multirotor Unmanned Aerial Vehicles," *AIAA Journal*, Vol. 57, No. 3, 2019, pp. 1250–1259. https://doi.org/10.2514/1.J057165

[12] McKay, M. E., Niemiec, R., and Gandhi, F., "Analysis of Classical and Alternate Hexacopter Configurations with Single Rotor Failure," *Journal of Aircraft*, Vol. 55, No. 6, 2018, pp. 2372–2379. https://doi.org/10.2514/1.C035005

[13] Selig, M. S., "Real-Time Flight Simulation of Highly Maneuverable Unmanned Aerial Vehicles," *Journal of Aircraft*, Vol. 51, No. 6, 2014, pp. 1705–1725. https://doi.org/10.2514/1.C032370

[14] Lee, D.-K., and Han, J.-H., "Safety-Guaranteed Flight Test Environment for Micro Air Vehicles," *AIAA Journal*, Vol. 54, No. 3, 2016, pp. 1018–1029. https://doi.org/10.2514/1.J054241

[15] Berning, A. W., Taheri, E., Girard, A., and Kolmanovsky, I., "Rapid Uncertainty Propagation and Chance-Constrained Trajectory Optimization for Small Unmanned Aerial Vehicles," *2018 Annual American Control Conference (ACC)*, IEEE, New York, 2018, pp. 3183–3188.

[16] Roshanian, J., Ebrahimi, M., Taheri, E., and Bataleblu, A. A., "Multidisciplinary Design Optimization of Space Transportation Control System Using Genetic Algorithm," *Proceedings of the Institution of Mechanical Engineers, Part G: Journal of Aerospace Engineering*, Vol. 228, No. 4, 2014, pp. 518–529. https://doi.org/10.1177/0954410013475573

[17] Kamyar, R., and Taheri, E., "Aircraft Optimal Terrain/Threat-Based Trajectory Planning and Control," *Journal of Guidance, Control, and Dynamics*, Vol. 37, No. 2, 2014, pp. 466–483. https://doi.org/10.2514/1.61339

[18] Kosovic, B., and Curry, J. A., "A Large Eddy Simulation Study of a Quasi-Steady, Stably Stratified Atmospheric Boundary Layer," *Journal of the Atmospheric Sciences*, Vol. 57, No. 8, 2000, pp. 1052–1068. https://doi.org/10.1175/1520-0469(2000)057<1052:ALESSO>2.0.CO;2

[19] Michalakes, J., Dudhia, J., Gill, D., Klemp, J., and Skamarock, W., "Design of a Next-Generation Regional Weather Research and Forecast Model," *Towards Teracomputing*, 1998, pp. 117–124.

[20] Dudhia, J., Gill, D., Henderson, T., Klemp, J., Skamarock, W., and Wang, W., "The Weather Research and Forecast Model: Software Architecture and Performance," *Proceedings of the Eleventh ECMWF Workshop on the Use of High Performance Computing in Meteorology*, World Scientific, Reading, U.K., Oct. 2004, pp. 156–168.

[21] Huang, H., Hoffmann, G. M., Waslander, S. L., and Tomlin, C. J., "Aerodynamics and Control of Autonomous Quadrotor Helicopters in Aggressive Maneuvering," *IEEE International Conference on*

**Data available online at https://github.com/behdad2018/FlightSim_QR_AIAA.

Robotics and Automation, 2009. ICRA'09, IEEE, New York, 2009, pp. 3277–3282.

[22] Ventura Diaz, P., and Yoon, S., "High-Fidelity Computational Aerodynamics of Multi-Rotor Unmanned Aerial Vehicles," *2018 AIAA Aerospace Sciences Meeting*, AIAA Paper 2018-1266, 2018.

[23] Thibault, S., Holman, D., Garcia, S., and Trapani, G., "CFD Simulation of a Quad-Rotor UAV with Rotors in Motion Explicitly Modeled Using an LBM Approach with Adaptive Refinement," *55th AIAA Aerospace Sciences Meeting*, AIAA Paper 2017-0583, 2017.

[24] Yoon, S., Ventura Diaz, P., Boyd, D. D., Jr., Chan, W. M., and Theodore, C. R., "Computational Aerodynamic Modeling of Small Quadcopter Vehicles," *American Helicopter Society (AHS) 73rd Annual Forum*, SKU 73-2017-0015, Fort Worth, TX, May 2017.

[25] Thom, A., and Duraisamy, K., "Computational Investigation of Unsteadiness in Propeller Wake–Wing Interactions," *Journal of Aircraft*, Vol. 50, No. 3, 2013, pp. 985–988. https://doi.org/10.2514/1.C031866

[26] Lakshminarayan, V., Bush, B., Duraisamy, K., and Baeder, J., "Computational Investigation of Micro Hovering Rotor Aerodynamics," *24th AIAA Applied Aerodynamics Conference*, AIAA Paper 2006-2819, 2006.

[27] Duraisamy, K., Ramasamy, M., Baeder, J. D., and Leishman, J. G., "High-Resolution Computational and Experimental Study of Rotary-Wing Tip Vortex Formation," *AIAA Journal*, Vol. 45, No. 11, 2007, pp. 2593–2602. https://doi.org/10.2514/1.26575

[28] Kim, H. W., Kenyon, A. R., Brown, R., and Duraisamy, K., "Interactional Aerodynamics and Acoustics of a Hingeless Coaxial Helicopter with an Auxiliary Propeller in Forward Flight," *Aeronautical Journal*, Vol. 113, No. 1140, 2009, pp. 65–78. https://doi.org/10.1017/S0001924000002797

[29] Singh, P., and Friedmann, P. P., "Application of Vortex Methods to Coaxial Rotor Wake and Load Calculations in Hover," *Journal of Aircraft*, Vol. 55, No. 1, 2018, pp. 373–381. https://doi.org/10.2514/1.C034520

[30] von Kármán, T., "Progress in the Statistical Theory of Turbulence," *Proceedings of the National Academy of Sciences*, Vol. 34, No. 11, 1948, pp. 530–539.

[31] Hoblit, F. M., *Gust Loads on Aircraft: Concepts and Applications*, AIAA, Reston, VA, 1988.

[32] Schiess, J. R., "Composite Statistical Method for Modeling Wind Gusts," *Journal of Aircraft*, Vol. 23, No. 2, 1986, pp. 131–135. https://doi.org/10.2514/3.45279

[33] Pope, S. B., *Turbulent Flows*, Cambridge Univ. Press, New York, 2001.

[34] Forrester, D. A., and Dean, G. C., "Improvement of Meteorological Data for Air Traffic Management Purposes," *Air Traffic Control Quarterly*, Vol. 2, No. 2, 1994, pp. 85–101. https://doi.org/10.2514/atcq.2.2.85

[35] Galway, D., Etele, J., and Fusina, G., "Modeling of Urban Wind Field Effects on Unmanned Rotorcraft Flight," *Journal of Aircraft*, Vol. 48, No. 5, 2011, pp. 1613–1620. https://doi.org/10.2514/1.C031325

[36] Moeng, C.-H., "A Large-Eddy-Simulation Model for the Study of Planetary Boundary-Layer Turbulence," *Journal of the Atmospheric Sciences*, Vol. 41, No. 13, 1984, pp. 2052–2062. https://doi.org/10.1175/1520-0469(1984)041<2052:ALESMF>2.0.CO;2

[37] Moeng, C.-H., "Large-Eddy Simulation of a Stratus-Topped Boundary Layer. Part I: Structure and Budgets," *Journal of the Atmospheric Sciences*, Vol. 43, No. 23, 1986, pp. 2886–2900. https://doi.org/10.1175/1520-0469(1986)043<2886:LESOAS>2.0.CO;2

[38] Khanna, S., and Brasseur, J. G., "Analysis of Monin–Obukhov Similarity from Large-Eddy Simulation," *Journal of Fluid Mechanics*, Vol. 345, Aug. 1997, pp. 251–286. https://doi.org/10.1017/S0022112097006277

[39] Jayaraman, B., and Brasseur, J., "Transition in Atmospheric Turbulence Structure from Neutral to Convective Stability States," *32nd ASME Wind Energy Symposium*, AIAA Paper 2014-0868, 2014.

[40] Jayaraman, B., and Brasseur, J. G., "Transition in Atmospheric Boundary Layer Turbulence Structure from Neutral to Moderately Convective Stability States and Implications to Large-Scale Rolls," arXiv preprint arXiv:1807.03336, 2018.

[41] Johansson, C., Smedman, A.-S., Högström, U., Brasseur, J. G., and Khanna, S., "Critical Test of the Validity of Monin–Obukhov Similarity During Convective Conditions," *Journal of the Atmospheric Sciences*, Vol. 58, No. 12, 2001, pp. 1549–1566. https://doi.org/10.1175/1520-0469(2001)058<1549:CTOTVO>2.0.CO;2

[42] Brasseur, J. G., and Wei, T., "Designing Large-Eddy Simulation of the Turbulent Boundary Layer to Capture Law-of-the-Wall Scaling," *Physics of Fluids*, Vol. 22, No. 2, 2010, Paper 021303. https://doi.org/10.1063/1.3319073

[43] Berkooz, G., Holmes, P., and Lumley, J. L., "The Proper Orthogonal Decomposition in the Analysis of Turbulent Flows," *Annual Review of Fluid Mechanics*, Vol. 25, No. 1, 1993, pp. 539–575. https://doi.org/10.1146/annurev.fl.25.010193.002543

[44] *Flying Qualities of Piloted Aircraft*, Department of Defense Handbook, MIL-HDBK-1797B, U.S. Department of Defense, Washington, D.C., 2012.

[45] Mishra, A., Davoudi, B., and Duraisamy, K., "Multiple-Fidelity Modeling of Interactional Aerodynamics," *Journal of Aircraft*, Vol. 55, No. 5, 2018, pp. 1839–1854. https://doi.org/10.2514/1.C034709

[46] Leishman, J. G., *Principles of Helicopter Aerodynamics*, 2nd ed., Cambridge Univ. Press, New York, 2006.

[47] Beard, R. W., and McLain, T. W., *Small Unmanned Aircraft: Theory and Practice*, Princeton Univ. Press, Princeton, NJ, 2012.

[48] Sharma, P., and Atkins, E. M., "An Experimental Investigation of Tractor and Pusher Hexacopter Performance," *2018 Atmospheric Flight Mechanics Conference*, AIAA Paper 2018-2983, 2018.

[49] Bangura, M., "Aerodynamics and Control of Quadrotors," Doctor of Philosophy, The Australian National Univ., 2017.

[50] Schaub, H., and Junkins, J. L., *Analytical Mechanics of Space Systems*, AIAA, Reston, VA, 2003, Chap. 1.

[51] Zuo, Z., "Trajectory Tracking Control Design with Command-Filtered Compensation for a Quadrotor," *IET Control Theory & Applications*, Vol. 4, No. 11, 2010, pp. 2343–2355. https://doi.org/10.1049/iet-cta.2009.0336

[52] Koehl, A., Rafaralahy, H., Boutayeb, M., and Martinez, B., "Aerodynamic Modelling and Experimental Identification of a Coaxial-Rotor UAV," *Journal of Intelligent & Robotic Systems*, Vol. 68, No. 1, 2012, pp. 53–68. https://doi.org/10.1007/s10846-012-9665-x

[53] Taheri, E., and Abdelkhalik, O., "Shape Based Approximation of Constrained Low-Thrust Space Trajectories Using Fourier Series," *Journal of Spacecraft and Rockets*, Vol. 49, No. 3, 2012, pp. 535–546.

A. R. Jones
Associate Editor